Geophysical Journal International

Geophys. J. Int. (2013) **192,** 230–247 doi: 10.1093/gji/ggs006

A hybrid method to compute short-period synthetic seismograms of teleseismic body waves in a 3-D regional model

Vadim Monteiller,[1,2] Sébastien Chevrot,[1] Dimitri Komatitsch[2] and Nobuaki Fuji[1]

[1] *Institut de Recherche an Astrophysique et Planétologie, Observatoire Midi-Pyrénées, CNRS, UMR* 5277, *Université Paul Sabatier, Toulouse, France. E-mail: chevrot@dtp.obs-mip.fr*

[2] *LMA, CNRS, UPR* 7051*, Aix-Marseille University, Centrale Marseille,* 13402 *Marseille Cedex* 20, *France*

Accepted 2012 October 4. Received 2012 September 27; in original form 2012 March 27

SUMMARY

We present a hybrid method to simulate the propagation of short-period teleseismic body waves through 3-D regional models. The incident wavefield is computed in an spherically symmetric reference earth model based on the direct solution method. The global and regional wavefields are matched at the boundaries of the regional mesh. In the regional domain, we implement a spectral-element method with absorbing boundaries to cancel the outgoing scattered wavefield. The hybrid method is successfully benchmarked against the direct solution method in the reference earth model iasp91. The potential of the method is illustrated by computing short-period *P*-wave synthetic seismograms in a 3-D model with a 20 km Moho offset and/or topography on the free surface, focusing on the actual example of the Pyrenees.

Key words: Body waves; Computational seismology; Wave scattering and diffraction; Wave propagation.

1 INTRODUCTION

In the last decade, deployments of dense regional arrays such as the USArray transportable array have considerably improved our capacity to image the interior of the Earth. However, the exploitation of the wealth of information coming from these new and large amounts of high-quality broadband data still heavily relies on asymptotic approaches. For example, most regional body wave tomographies are still performed within the framework of asymptotic ray theory (e.g. Burdick *et al.* 2008; Roth *et al.* 2008), a practice that dates back to the pioneering work of Aki *et al.* (1977). For the sake of efficiency, the few finite-frequency tomography studies at the regional scale (e.g. Hung *et al.* 2004; Sigloch *et al.* 2008) all used sensitivity kernels computed with the asymptotic approach introduced by Dahlen *et al.* (2000), thus neglecting the near-field effects that are important in the vicinity of seismological stations (Favier *et al.* 2004). In addition, their computations were performed in a spherically symmetric reference earth model. In principle, these shortcomings can be overcome by recently developed full-wave approaches (e.g. Akçelic *et al.* 2003; Fichtner *et al.* 2008; Liu & Tromp 2008; Tromp *et al.* 2008) but these methods still suffer from a heavy computational cost, which limits their application to periods larger than a few seconds only, even at the regional scale (Tape *et al.* 2009). Migration of receiver functions (e.g. Bostock *et al.* 2001, 2002; Audet *et al.* 2009) to obtain fine images of internal discontinuities such as the Moho or the lithosphere–asthenosphere boundary is another rapidly developing field for which the benefit of using dense regional deployments is the most rewarding. However, these imaging approaches still extensively rely on asymptotic theories to obtain migrated images and do not fully account for all the complexity that may affect wave propagation in 3-D media.

Various efforts to close the gap between tomographic imaging based upon ray theory and waveform inversion at the regional scale have been reported in a number of studies. For example, Wen & Helmberger (1998) developed a hybrid method combining generalized ray theory for propagation in the global Earth and finite differences in a 2-D Cartesian rectangular region near the core–mantle boundary. A similar approach was later used to model wave propagation in a 2-D heterogeneous and anisotropic upper mantle Zhao *et al.* (2008). While these methods are efficient, they suffer from serious limitations such as considering 2-D heterogeneous domains with a Cartesian geometry. More recently, Roecker *et al.* (2010) modelled the propagation of an incident plane wave based on finite differences in a 2.5-D heterogeneous domain. This approach neglects the sphericity of the Earth and the curvature of the incident wave front. In addition, since it is restricted to problems with a cylindrical symmetry, its potential for exploiting real data sets is limited. A 3-D hybrid method involving coupling between the spectral-element method (SEM) in an outer 3-D spherical shell and a normal-mode solution method in an inner sphere was proposed by Capdeville *et al.* (2003). Since full normal-mode catalogues are very difficult to compute accurately below 8 s, this method is well adapted for problems involving long-period surface waves but less so for short-period teleseismic body waves. A first attempt at developing a 3-D hybrid method to model teleseismic body waves in a regional domain is reported in Chevrot *et al.* (2004).

In that study, a spectral-element method was used in a regional mesh to model the propagation of SKS waves through heterogeneous anisotropic media. However, that approach is also severely limited by the fact that the regional domain is embedded inside a homogeneous background medium and that the incoming wave fronts are planar.

From this short overview, it is clear that efficient numerical methods that would allow seismologists to model short-period teleseismic body waves in 3-D media are strongly needed, if they are to perform waveform inversion of seismograms recorded by dense regional broadband arrays. Hereafter, we present such a method, and we carefully validate and benchmark it versus the direct solution method (DSM) in the reference earth model iasp91. We then illustrate its potential by computing synthetic seismograms in models with a 20 km Moho offset and/or topography at the free surface for an actual example taken in the Pyrenees.

2 THEORY AND OUTLINE OF THE METHOD

Domain Reduction Methods are particularly attractive when the source is located far from the local structures and if one wants to perform a sequence of simulations for this source with variable local structures. This property has been extensively exploited, for example, to investigate site effects resulting from topography (e.g. Bouchon *et al.* 1996) or sedimentary basins (e.g. Yoshimura *et al.* 2003). It is also particularly relevant in high-resolution imaging based upon waveform inversion of teleseismic body waves at the regional scale, an aspect that has so far received comparably little attention from the seismological community. In this case, the main difficulty is to compute exact synthetic seismograms in the global Earth for periods as short as 1 s, which are still beyond the reach of 3-D modelling at the global scale. Indeed, the current practical limit for a few simulations performed on large clusters of computers is around 5 s (e.g. Komatitsch *et al.* 2008, 2010) and the current maximum for a single run on the largest computers in the world is around 2 s (Carrington *et al.* 2008), while the resolution of an iterative inverse problem would typically involve hundreds to thousands of runs. In this study, we have thus decided to couple a 1-D global method to a 3-D regional method. Each method provides very accurate solutions of the wave equation in its own domain of validity, and the problem is thus to make the global and regional wavefields match on the boundaries of the regional mesh. The coupling approach we develop is general. Should the 3-D computations at the global scale become feasible, it would be straightforward to replace the incident wavefield computed in a spherically symmetric earth model by the incident wavefield computed in a 3-D global model. The benefit of the hybrid method would still be important because it would restrict the later computations inside the limited regional domain, which would considerably speed up the computations of synthetic seismograms, a critical point in the perspective of iterative waveform inversion. In any case, contributions of 3-D global propagation effects are expected to be small, especially for waves having their turning well above the CMB, because the teleseismic waves that reach the regional domain are produced by very distant sources and follow almost identical paths. Therefore, they sense little, if any, heterogeneities outside the regional domain. In the following, we review the advantages and shortcomings of the most widely used techniques to compute synthetic seismograms in spherically symmetric earth models, and justify our choice to use the DSM, which is a Galerkin method introduced by Geller & Ohminato (1994).

2.1 Numerical methods to compute synthetic seismograms in a spherically symmetric earth model

The development of methods to compute synthetic seismograms in a spherical earth model has a long history. The computation of normal modes initiated in the late fifties (Alterman *et al.* 1959). Since then, normal-mode summation has been widely used to compute long-period synthetic seismograms, which are essential ingredients in the inversion of moment tensor solutions (Dziewonski *et al.* 1981) and in the determination of the spherical and aspherical structure of the Earth (Dziewonski & Anderson 1981; Woodhouse & Dziewonski 1984). This approach is still widely used in surface wave tomography at both global and regional scales (e.g. Chevrot & Zhao 2007; Ritsema *et al.* 2011). Its main advantage is that it provides exact synthetic seismograms, including the effects of anelasticity, Earth's rotation and gravity, for a small computational cost. Its main shortcomings are that the computation of spheroidal modes at periods below 8 s is difficult (e.g. Al Attar & Woodhouse, 2008), and that the number of modes that need to be summed increases dramatically with frequency. Thus, while normal mode methods are ideally suited to the computation of long-period seismograms, they are not suited to modelling short-period teleseismic body-wave records.

To compute solutions of the wave equation at short period, different techniques have been proposed, which involve different types of approximations. Both the generalized ray theory (e.g. Helmberger 1974) and WKBJ method (e.g. Chapman & Orcutt 1985) rely on ray expansions. Therefore, these methods are very efficient for computing short-period synthetic seismograms. However, they fail in shadow zones and for ray turning points close to an internal discontinuity. In addition, they necessitate identification and summation of all the rays that contribute to a slowness integral, which complicates their implementation. Full-wave theory (Richards 1973) avoids some of the drawbacks of the WKBJ method. However, it involves the evaluation of complex integrals along a contour in the complex slowness plane which needs to be defined *a priori* for each particular phase and frequency. The reflectivity method (Fuchs & Müller 1971) provides nearly complete solutions in spherically symmetric earth models but relies on an Earth-flattening transformation that is exact for SH waves but not for *P* and *SV* waves. To summarize, while these approaches are all very efficient from a computational point of view, they do not always provide exact or complete solutions of the wave equation. In addition, their implementation can be cumbersome and needs to be tuned for each part of the seismic wavefield of interest.

In the nineties, new methods were developed to obtain very accurate solutions of the seismic wave equation in a spherical Earth model. These solutions give a set of expansion coefficients of the displacement vector in the basis of vector spherical harmonics. The DSM is a Galerkin method that solves the weak form of the equation of motion in the frequency domain (e.g. Geller & Ohminato 1994; Geller & Takeuchi 1995; Kawai *et al.* 2006). By carefully tuning the vertical grid spacing, maximum angular order and cut-off depth, the calculations can be made efficient while keeping high accuracy, even at frequencies as high as 2 Hz (Kawai *et al.* 2006). The GEMINI method (Green functions of the Earth by MINor Integration) directly solves for the expansion coefficients of displacement by numerically integrating spherical systems of coupled first-order ordinary differential equations with respect to the vertical coordinate using second-order minors (Friederich & Dalkolmo 1995). Both methods provide expansion coefficients of displacement in the Fourier domain as a function of radial and angular

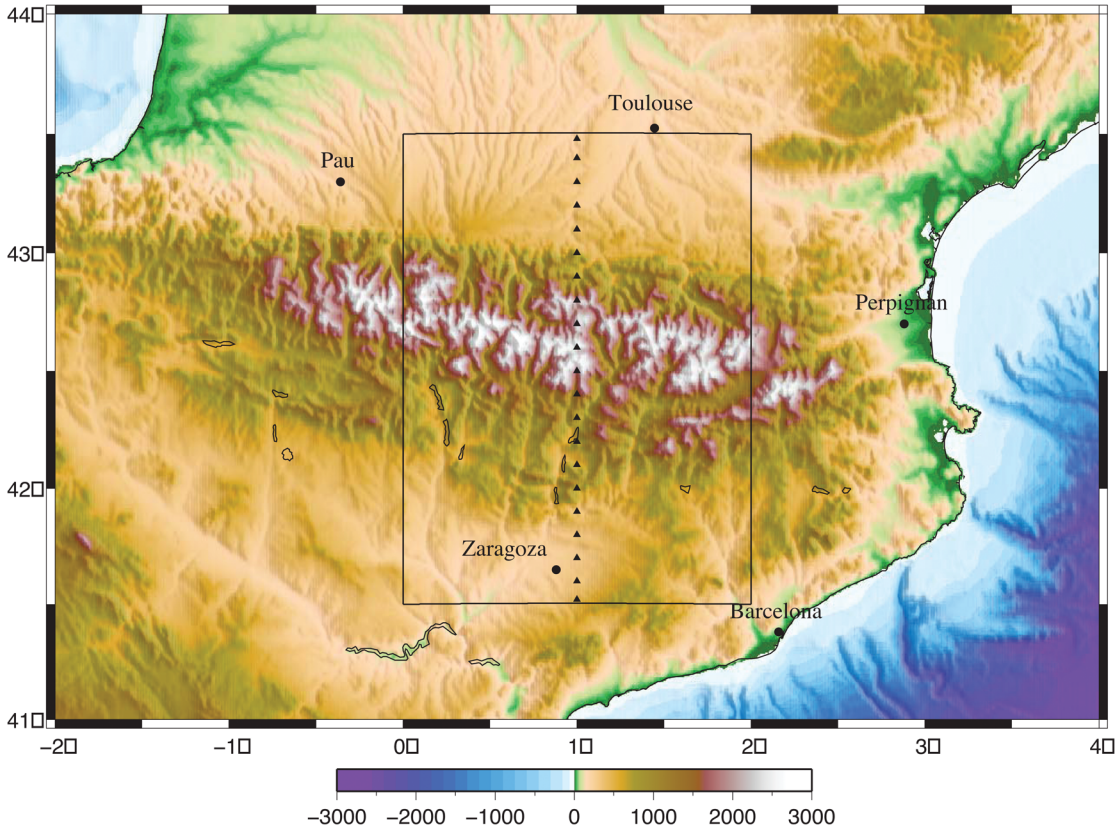

Figure 1. Spectral-element 2° × 2° regional grid with the topography of the Pyrenees taken from etopo1. The receivers are positioned along an N–S profile with an interstation spacing of 0.1°.

orders. In the following, we will focus on the DSM method and describe the different steps required to couple the global and regional domains.

2.2 SEM for 3-D seismic wave propagation inside the regional domain

In the 3-D regional domain, we use a spectral-element method (SEM) (e.g. Tromp *et al.* 2008), which is a highly accurate technique to model seismic wave propagation in elastic or anelastic media. The SEM is based upon the variational (or weak) form of the seismic wave equation. Because it uses high-degree polynomial basis functions, can handle very distorted meshes (Oliveira & Seriani 2011) and does not necessitate interpolation of material properties, it is highly accurate and allows one to include all the complexity that may affect the seismic wavefields: topography of the free surface and of internal discontinuities, anelasticity, anisotropy and lateral variations of elastic parameters and density. The SEM is a continuous Galerkin technique, which can easily be made discontinuous (see e.g. Wilcox *et al.* 2010 for a review); it is then close to a particular case of the discontinuous Galerkin technique (see e.g. Falk & Richter 1999; Hu *et al.* 1999; Rivière & Wheeler 2003) in the context of seismic wave modelling), with optimized efficiency because of its tensorized basis functions. Note that in most geological models in the context of seismic wave propagation studies (except for fault dynamic rupture studies), a discontinuous mesh is not needed because material property contrasts are not drastic, and thus a continuous formulation is sufficient. This is particularly true at the scale of the full Earth.

2.3 Coupling 1-D global and 3-D regional numerical modelling techniques

The 3-D regional mesh is embedded in a spherically symmetric global earth model. To simulate seismic wave propagation in that regional mesh, we need to introduce the incident wavefield generated by the distant source that has propagated through the global model, and we also need to absorb the outgoing waves diffracted by the 3-D regional model. To do so, we implement a simplified version of the method suggested by Bielak & Christiano (1984), in which absorbing boundary conditions are applied to the diffracted field only. We write the total displacement vector $\mathbf{u}$ as the sum of the incident wavefield $\mathbf{u_0}$ and of the diffracted wavefield $\mathbf{u_d}$. The incident wavefield is computed based upon DSM at all the grid points on the edges of the regional domain in the global 1-D model. There is no upper frequency limit in the spectral-element part of the calculation, and thus the only upper limit of the hybrid technique is the highest frequency that the DSM technique can compute, i.e. about 2 Hz. We compute the total field in the mesh using the SEM and then apply the absorbing boundary condition to $\mathbf{u_d} = \mathbf{u} - \mathbf{u_0}$. We currently use paraxial absorbing boundary conditions (Stacey 1988), the efficiency of which, as will be shown in the following, is quite satisfactory. Note that more efficient convolution perfectly matched layers (C-PMLs) absorbing layers could be used if necessary (see e.g. Martin *et al.* 2008).

Implementing paraxial absorbing conditions to the diffracted field only implies knowing both traction and velocities produced by the incident wavefield on the absorbing boundaries of the grid, because they must be subtracted from the total field before applying the

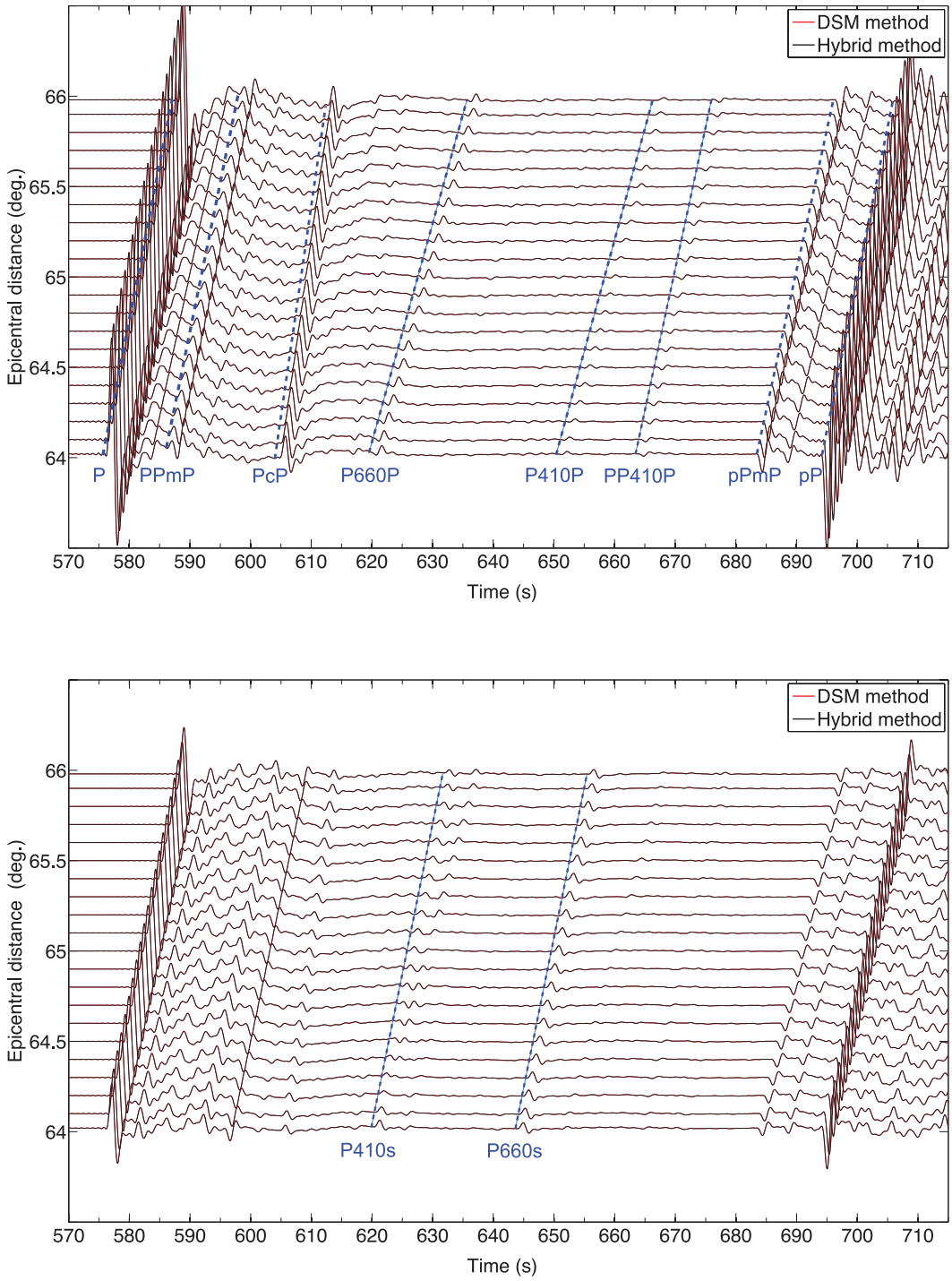

Figure 2. Vertical (top) and radial (bottom) components of synthetic seismograms computed by the hybrid method (black lines) and by the DSM (red lines) in the reference earth model iasp91 for an explosive source located at 600 km depth.

absorbing conditions. Both are easily computed with DSM as described below because by construction of our coupling technique, the material properties along those boundaries are those of the 1-D global model.

2.4 Computation of traction in the global spherical model

The DSM computes the solution of the weak form of the equation of motion by directly solving the Galerkin weak form of the equation of motion (e.g. Takeuchi & Saito 1972; Kawai *et al.* 2006):

$$(\omega^2\mathbf{T} - \mathbf{H} + \mathbf{R})\mathbf{c} = -\mathbf{g}, \tag{1}$$

where $\mathbf{T}$ is the mass matrix, $\mathbf{H}$ is the stiffness matrix, $\mathbf{g}$ is the force vector and $\mathbf{R}$ is the matrix operator corresponding to the natural boundary condition. The explicit form of the matrix and vector elements is

$$T_{mn} = \int_V \left(\phi_i^{(m)}\right)^* \rho \phi_i^{(n)} dV, \tag{2}$$

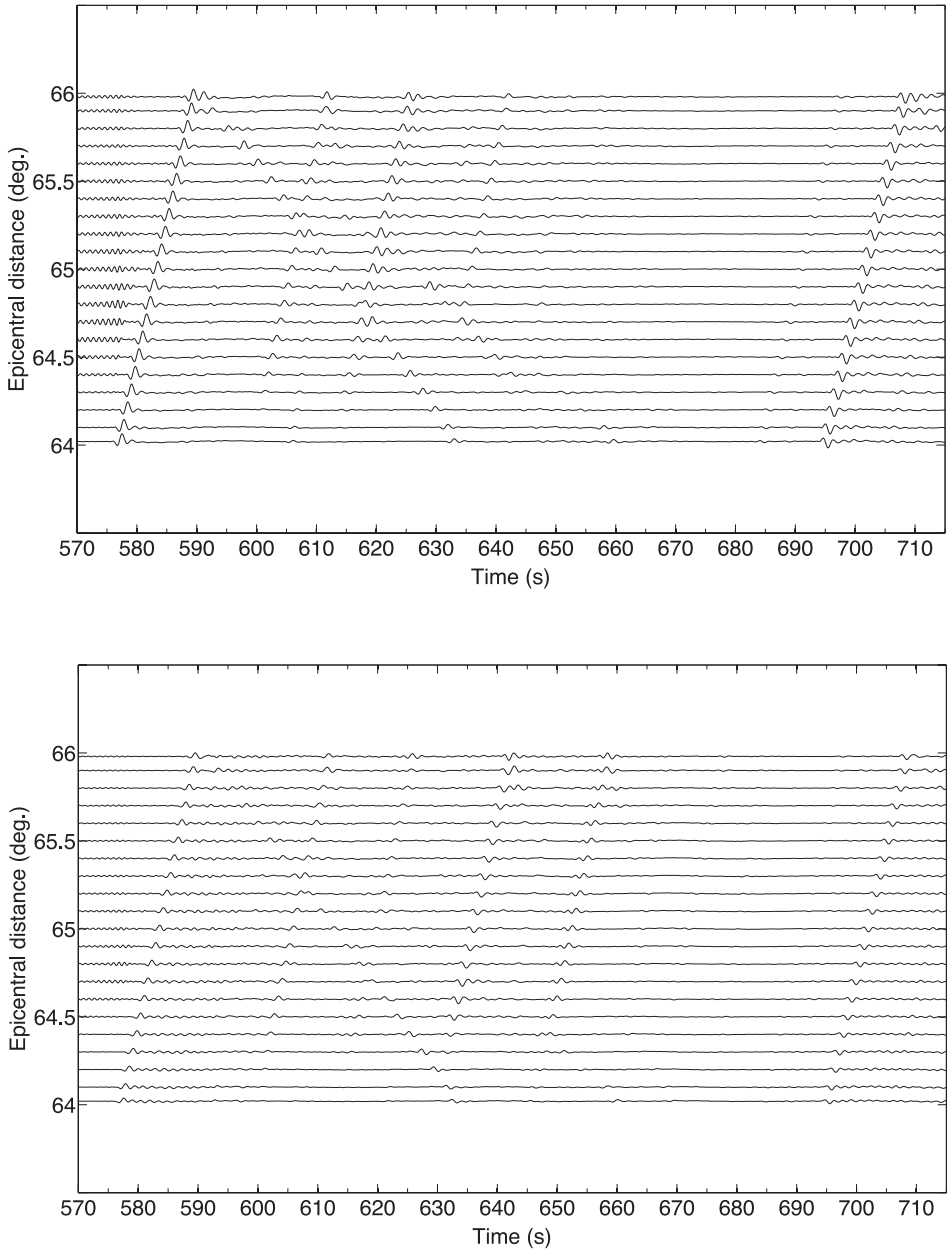

Figure 3. Differences between the vertical (top) and radial (bottom) synthetic seismograms computed by the hybrid method and by the DSM shown in Fig. 2, exaggerated by a factor of 10.

$$H_{mn} = \int_V \left(\phi_{i,j}^{(m)}\right)^* C_{ijkl} \phi_{k,l}^{(n)} dV, \tag{3}$$

$$R_{mn} = \int_S \left(\phi_i^{(m)}\right)^* S_{ij} \phi_j^{(n)} dS, \tag{4}$$

$$g_m = \int_V \left(\phi_i^{(m)}\right)^* f_i dV, \tag{5}$$

where ρ and C_{ijkl} are, respectively, the density scalar and stiffness tensor, and $\mathbf{f}$ the excitation of the source. The displacement vector is then given by a linear combination of N vector trial functions $\phi_i(n)$:

$$u_i(\mathbf{r}) = \sum_{n=1}^{N} c_n \phi_i(n)(\mathbf{r}). \tag{6}$$

We use linear interpolation functions $X_k(r)$ to describe the vertical variation of displacement:

$$X_k(r) = \begin{cases} (r - r_{k-1})/(r_k - r_{k-1}) & : \quad r_{k-1} < r \leq r_k, \\ (r_{k+1} - r)/(r_{k+1} - r_k) & : \quad r_k \leq r < r_{k+1}, \\ 0 & : \quad \text{otherwise}, \end{cases} \tag{7}$$

and complex vector spherical harmonics $\mathbf{S}_{lm}^1$, $\mathbf{S}_{lm}^2$ and $\mathbf{T}_{lm}$ to describe the lateral variation of displacement:

$$\mathbf{S}_{lm}^1(\theta, \phi) = (Y_{lm}(\theta, \phi), 0, 0),$$

$$\mathbf{S}_{lm}^2(\theta, \phi) = \left(0, \frac{1}{\mathcal{L}} \frac{\partial Y_{lm}(\theta, \phi)}{\partial \theta}, \frac{1}{\mathcal{L} \sin\theta} \frac{\partial Y_{lm}(\theta, \phi)}{\partial \phi}\right),$$

$$\mathbf{T}_{lm}(\theta, \phi) = \left(0, \frac{1}{\mathcal{L} \sin\theta} \frac{\partial Y_{lm}(\theta, \phi)}{\partial \phi}, -\frac{1}{\mathcal{L}} \frac{\partial Y_{lm}(\theta, \phi)}{\partial \theta}\right),$$

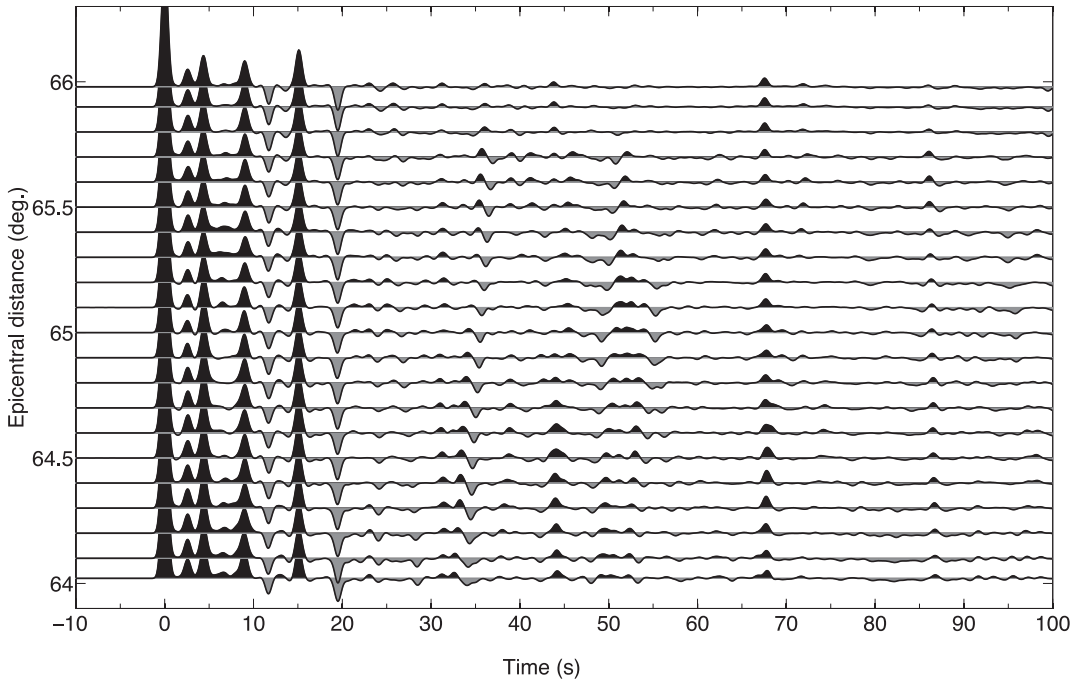

Figure 4. Receiver functions in iasp91 for the line of receivers shown in Fig. 1.

where $Y_{lm}(\theta, \phi)$ are the fully normalized spherical harmonics

$$Y_{lm}(\theta,\phi) = (-1)^m \left(\frac{2l+1}{4\pi}\right)^{1/2} \left[\frac{(l-m)!}{(l+m)!}\right]^{1/2} P_{lm}(\cos\theta) e^{im\phi}, \tag{8}$$

and $\mathcal{L} = \sqrt{l(l+1)}$ (Takeuchi & Saito 1972).

In this vector spherical harmonics basis, the displacement vector is given by

$$\mathbf{u}(r,\theta,\phi) = \sum_{lm} U_{lm}(r)\mathbf{S}^1_{lm} + V_{lm}(r)\mathbf{S}^2_{lm} + W_{lm}(r)\mathbf{T}_{lm}, \tag{9}$$

where the radial functions are related to the radial trial functions through:

$$U_{lm}(r) = \sum_k c^1_{lmk} X_k(r), \tag{10}$$

$$V_{lm}(r) = \sum_k c^2_{lmk} X_k(r), \tag{11}$$

$$W_{lm}(r) = \sum_k c^3_{lmk} X_k(r). \tag{12}$$

Once the displacement is obtained, we can compute the partial derivatives of displacement with respect to r, θ and ϕ as follows:

$$\frac{\partial}{\partial r}\mathbf{u}(r,\theta,\phi) = \sum_{lm} \frac{dU_{lm}(r)}{dr}\mathbf{S}^1_{lm} + \frac{dV_{lm}(r)}{dr}\mathbf{S}^2_{lm} + \frac{dW_{lm}(r)}{dr}\mathbf{T}_{lm}, \tag{13}$$

$$\frac{\partial}{\partial \theta}\mathbf{u}(r,\theta,\phi) = \sum_{lm} U_{lm}(r)\frac{\partial}{\partial\theta}\mathbf{S}^1_{lm} + V_{lm}(r)\frac{\partial}{\partial\theta}\mathbf{S}^2_{lm} + W_{lm}(r)\frac{\partial}{\partial\theta}\mathbf{T}_{lm}, \tag{14}$$

$$\frac{\partial}{\partial \phi}\mathbf{u}(r,\theta,\phi) = \sum_{lm} U_{lm}(r)\frac{\partial}{\partial\phi}\mathbf{S}^1_{lm} + V_{lm}(r)\frac{\partial}{\partial\phi}\mathbf{S}^2_{lm} + W_{lm}(r)\frac{\partial}{\partial\phi}\mathbf{T}_{lm}. \tag{15}$$

The derivatives of the trial functions $\mathbf{S}^1_{lm}$, $\mathbf{S}^2_{lm}$ and $\mathbf{T}_{lm}$ with respect to ϕ and θ are obtained analytically, using the following identities:

$$\frac{\partial Y_{lm}}{\partial\phi} = imY_{lm} \tag{16}$$

and

$$\frac{dP_{lm}}{d\theta} = m\frac{\cos\theta}{\sin\theta}P_{lm} - P_{lm-1}. \tag{17}$$

To obtain the derivatives of displacement with respect to the radial direction, we first interpolate the displacement with polynomials of degree 2. We then use the polynomial coefficients to compute the partial derivatives along the radial direction. To obtain the tractions on the edges of the regional 3-D domain, we first need to compute the strain from the displacement using (Takeuchi & Saito 1972):

$$\epsilon_{rr} = \frac{\partial u_r}{\partial r}, \tag{18}$$

$$\epsilon_{\theta\theta} = \frac{1}{r}\frac{\partial u_\theta}{\partial\theta} + \frac{1}{r}u_r, \tag{19}$$

$$\epsilon_{\phi\phi} = \frac{1}{r\sin\theta}\frac{\partial u_\phi}{\partial\phi} + \frac{1}{r}u_\theta\cot\theta + \frac{1}{r}u_r, \tag{20}$$

$$\epsilon_{r\theta} = \frac{\partial u_\theta}{\partial r} - \frac{1}{r}u_\theta + \frac{1}{r}\frac{\partial u_r}{\partial\theta}, \tag{21}$$

$$\epsilon_{r\phi} = \frac{1}{r\sin\theta}\frac{\partial u_r}{\partial\phi} + \frac{\partial u_\phi}{\partial r} - \frac{1}{r}u_\phi, \tag{22}$$

$$\epsilon_{\theta\phi} = \frac{1}{r}\frac{\partial u_\phi}{\partial\theta} - \frac{1}{r}u_\phi\cot\theta + \frac{1}{r\sin\theta}\frac{\partial u_\theta}{\partial\phi}. \tag{23}$$

We then obtain the components of the stress tensor:

$$\sigma_{rr} = (\lambda+2\mu)\epsilon_{rr} + \lambda(\epsilon_{\theta\theta} + \epsilon_{\phi\phi}), \tag{24}$$

$$\sigma_{\theta\theta} = \lambda\epsilon_{rr} + (\lambda+2\mu)(\epsilon_{\theta\theta} + \epsilon_{\phi\phi}) - 2\mu\epsilon_{\phi\phi}, \tag{25}$$

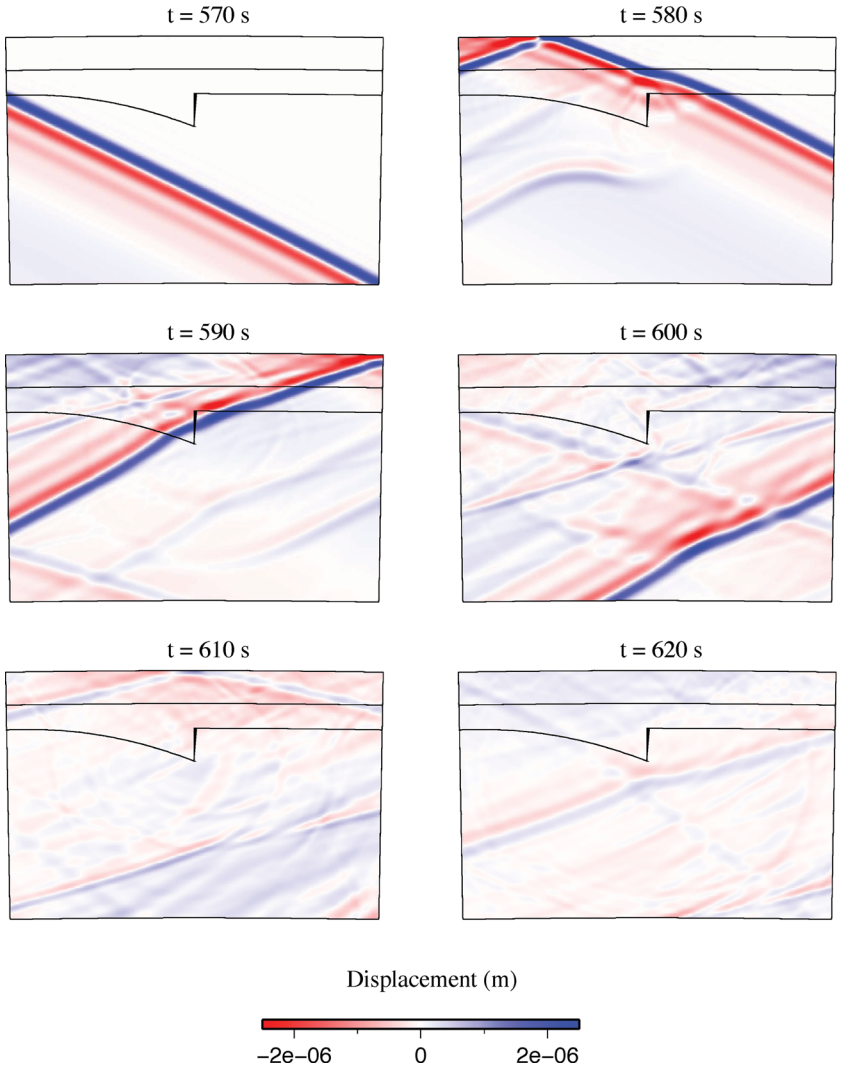

Figure 5. Snapshots of the vertical component of the total wavefield in the model with a 20 km Moho offset observed in the vertical great-circle plane.

$$\sigma_{\phi\phi} = \lambda\epsilon_{rr} + (\lambda + 2\mu)(\epsilon_{\theta\theta} + \epsilon_{\phi\phi}) - 2\mu\epsilon_{\theta\theta}, \quad (26)$$

$$\sigma_{\theta\phi} = \mu\epsilon_{\theta\phi}, \quad (27)$$

$$\sigma_{\phi r} = \mu\epsilon_{\phi r}, \quad (28)$$

$$\sigma_{r\theta} = \mu\epsilon_{r\theta}, \quad (29)$$

from which we can compute the traction $\mathbf{t} = \sigma \cdot \mathbf{n}$ on any surface defined by its unit normal $\mathbf{n}$. The components of traction are then projected from the geocentric reference frame to the regional SEM grid coordinate system. The three traction components of all the points located on the edges of the regional 3-D domain are computed once and for all and stored on a hard drive. They are read back at the beginning of each SEM run and stored in memory. A similar approach has been used to compute complete traveltime and amplitude sensitivity kernels for short-period teleseismic *P* waves in Fuji *et al.* (2012).

3 VALIDATION

Let us benchmark our hybrid method against the DSM in the iasp91 reference earth model (Kennett & Engdahl 1991). We consider an explosive source at 600 km depth, located 65° south of the centre of the regional grid shown in Fig. 1. The tractions and velocities are computed with DSM at frequencies up to 1.06 Hz, which requires summing the contribution and filtered with a low-pass Butterworth filter of order 6 and a cut-off frequency of 0.67 Hz, for all the nodes located on the edges of the regional grid (see, for example, Komatitsch & Tromp 1999 for a description of the mesh). In the DSM calculation, we consider a maximum angular order l such that the absolute values of the expansion coefficients are larger than 0.1 per cent of the maximum coefficient for each frequency at the free surface. For example, a 600 km deep earthquake requires summing the contribution of vector spherical harmonics to the vector displacement up to angular order 15 000 for a frequency of 1 Hz. The vertical grid spacing Δr to compute the tractions with DSM is given by

$$|\Delta r|^2 = \frac{12\beta^2(r)}{\omega^2} \times 10^{-3}, \quad (30)$$

where β is the shear wave velocity at radius r and ω the pulsation. We thus use a finer vertical grid spacing at higher frequency and in depth intervals where the shear wave velocity is smaller. The frequency content of our simulations reproduces the typical observation conditions of *P* receiver functions. The grid has a size of 2°

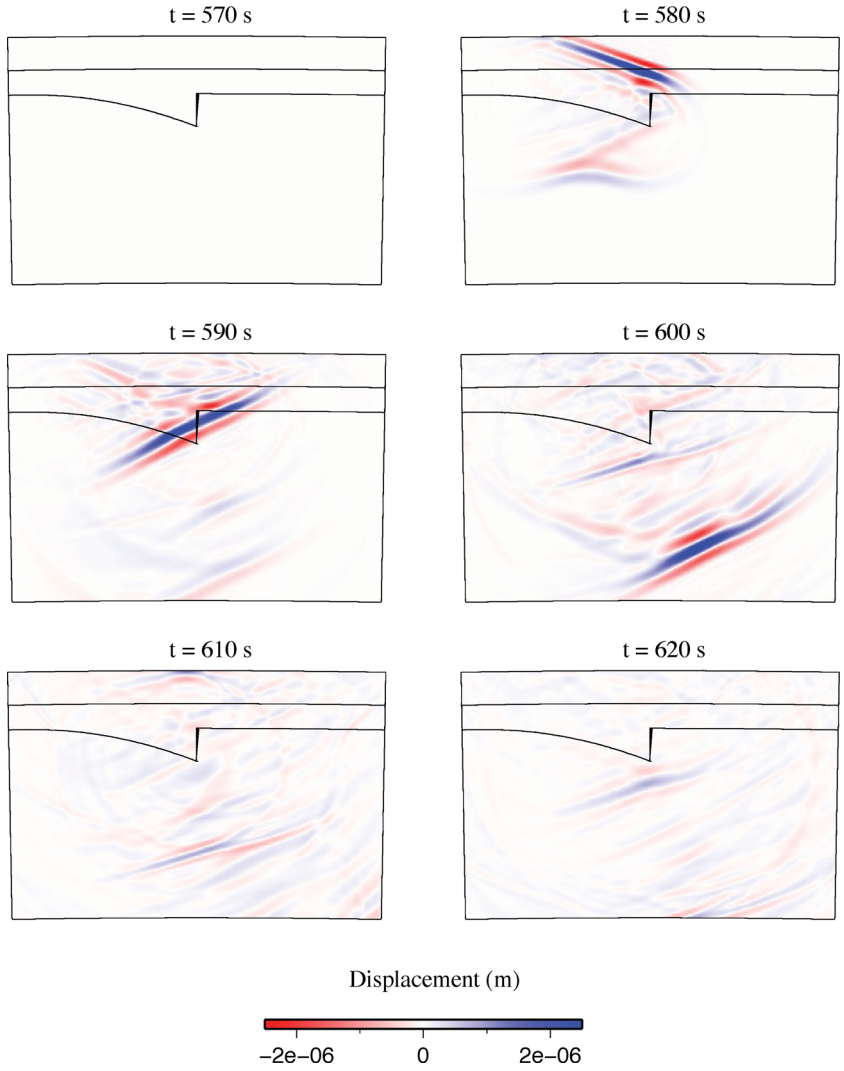

Figure 6. Snapshots of the vertical component of the scattered wavefield in the model with a 20 km Moho offset. The scattered wavefield is the difference between the total wavefield shown in Fig. 5 and the reference wavefield computed in model iasp91.

by 2° along the longitude and latitude dimensions and a thickness of 150 km. The number of elements is $90 \times 90 \times 60 = 486\,000$ and the time step is 1/40 s in all the simulations. The calculations for each of the test cases presented in the following took less than 1 hr of wall-clock time on a PC cluster using 30 processor cores for 10 000 time steps (250 s). For typical receiver function applications involving the *P* wave and its coda, a simulation duration of 60 s would be more than sufficient. This would require a computation time four times smaller (around 15 min), and even less if one is only interested in the *P* waveforms.

Fig. 2 shows the comparison of vertical and radial component synthetic seismograms recorded by receivers located along a N–S profile (Fig. 1). The agreement between the two independent computations is excellent for all the traces, including those located very close to the boundary of the mesh, and for the whole time interval, including the very late arrivals. The small discrepancies between DSM and the hybrid method (Fig. 3) are well below the level of scattered waves that we aim to model. Many seismic arrivals are observed in the coda of the *P* waves. Their identification is given in Fig. 2. Note that all the identifiable phases have interacted with an internal discontinuity (20 km, Moho, 410 km, and 660 km discontinuities) at most once, and many have also experienced an additional downward reflection beneath the free surface. Seismic phases that interact more than once with any internal discontinuity do exist but their amplitudes are much smaller and can thus be safely neglected.

For a better separation of seismic phases in the coda of the *P* wave, a common practice is to compute receiver functions by deconvolving the radial components from the vertical components (Langston 1979). Fig. 4 shows the receiver functions for stations along the N–S profile, obtained with the iterative deconvolution method of Ligorria & Ammon (1999). The *P*-to-*S* conversions on the crustal discontinuity at 20 km depth (hereafter referred to as the Conrad discontinuity) and on the Moho are now clearly separated and well resolved. They arrive, respectively, 2.5 and 4.0 s after the *P* wave. Their related multiples are also clearly identified at 9.0 and 12 s for the Conrad discontinuity and at 15.5 and 19.5 s for the Moho. Weaker phases are observed at 44 and 68 s. They correspond to the *P*-to-*S* conversions on the 410 and 660 km discontinuities, respectively. Note that the P410s is difficult to observe between 64.7° and 65.5°, owing to an interference with the P660P phase. Finally, the PP410P is also clearly detected around 87 s after the *P* wave, with a slowness very similar to that of the *P* wave. The P660s is also clearly detected at all the stations, contrary to the P410s.

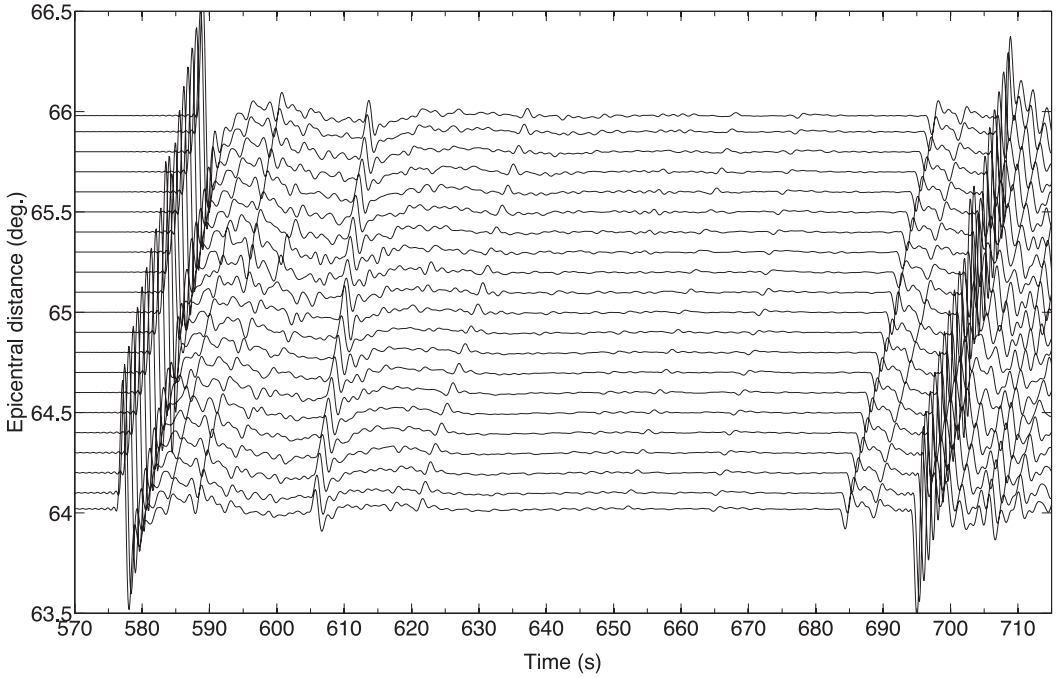

Figure 7. Vertical component synthetic seismograms in the model with a 20 km Moho offset for an explosive source located at 600 km depth.

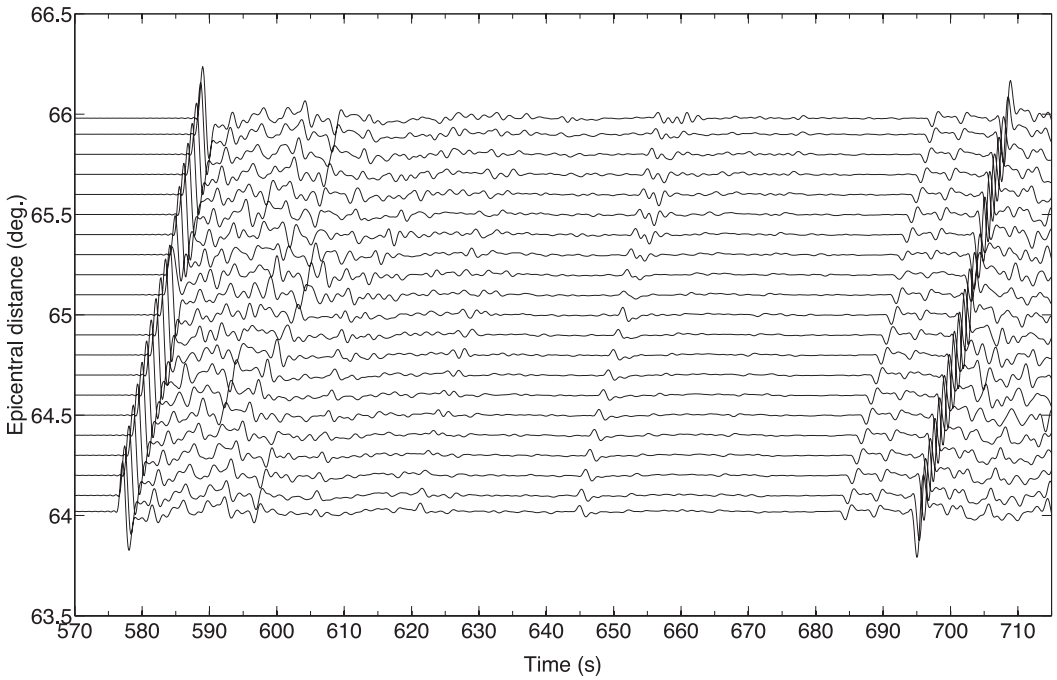

Figure 8. Radial component synthetic seismograms in the model with a 20 km Moho offset for an explosive source located at 600 km depth.

This observation emphasizes the need to consider a large number of events with varying epicentral distances for a robust detection of waves converted on deep discontinuities.

4 EXAMPLES OF COMPUTATIONS IN SIMPLE 3-D MODELS

We have now validated the hybrid method in the iasp91 reference earth model. In this section, let us now consider the effects of simple 3-D structures on *P* waveforms. In 1985 and 1986, the ECORS reflection profile was deployed across the Pyrenees to constrain a crustal model of the range (Choukroune *et al.* 1990). Data from the ECORS profile evidenced a strong Moho offset, located approximately beneath the North Pyrenean Fault, which corresponds to the former plate boundary between Iberia and Europe. Depending on the assumed crustal velocities, Daignières *et al.* (1989) estimated this Moho offset to be comprised between 15 and 20 km. In order to get a higher resolution picture of the structure of the

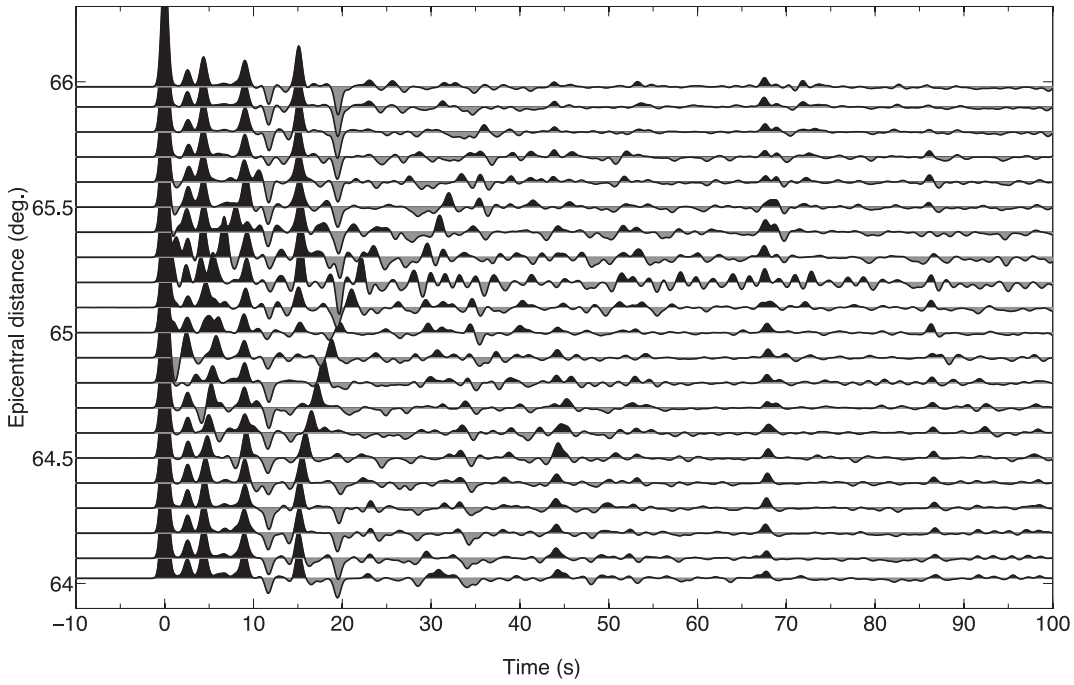

Figure 9. Receiver functions for the line of receivers shown in Fig. 1 when a Moho offset of 20 km on a vertical fault is included.

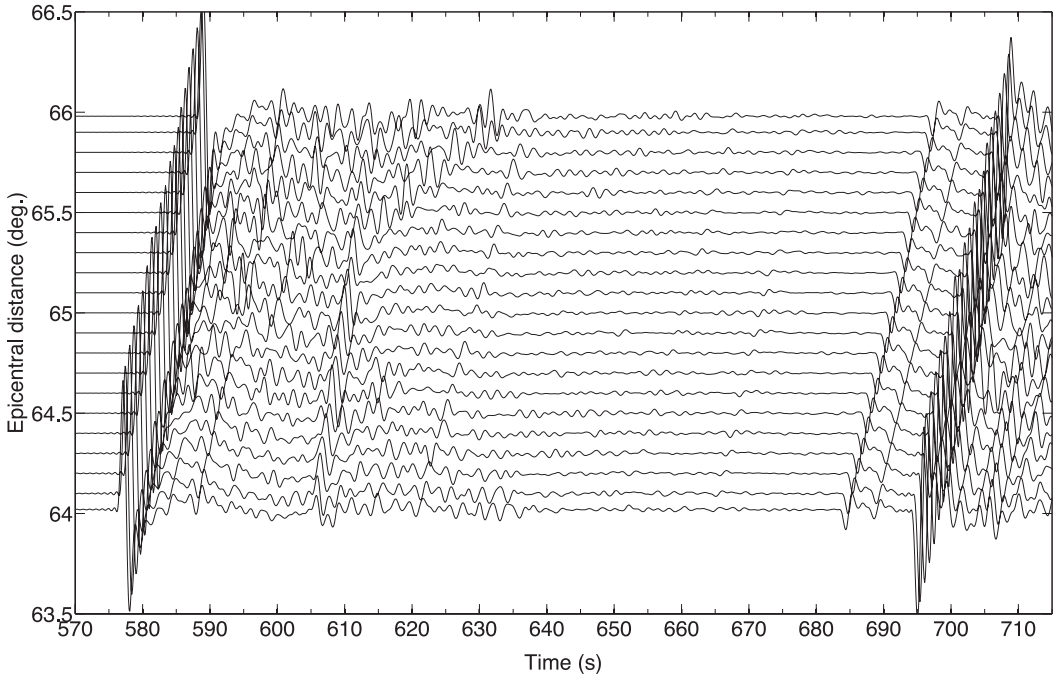

Figure 10. Vertical component synthetic seismograms in the model with the surface topography of the Pyrenees for an explosive source located at 600 km depth.

Pyrenees, in particular in the deeper parts of the crust and in the lithosphere, a dense transect across the Pyrenees is currently being deployed, roughly following the ECORS profile line. This transect is part of the PYROPE experiment, which will cover a much broader region, from the Pyrenees to the Massif Central. Since in the near future, we are interested in applying our hybrid method to exploit the data from this passive experiment, we consider two major features that may affect the seismological waveforms in this region: a Moho jump and/or topography of the free surface. In the following 3-D computations, the geometry of the experiment and the regional mesh are the same as in the validation case with the spherical reference earth model discussed in the previous section. However, we now use a cosine taper along the edges of the grid to suppress any structural discontinuity between the regional domain and the spherically symmetric background model that would generate artificial scattering. Movies of the total and scattered wavefields corresponding to the different cases can be found in the supporting information.

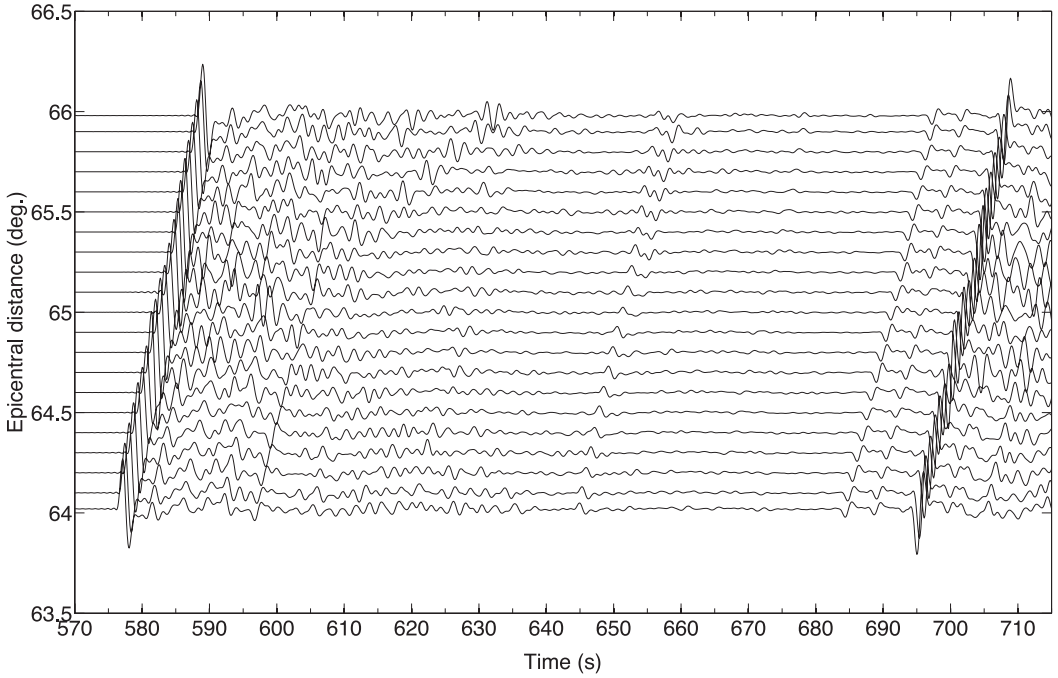

Figure 11. Radial component synthetic seismograms in the model with the surface topography of the Pyrenees for an explosive source located at 600 km depth.

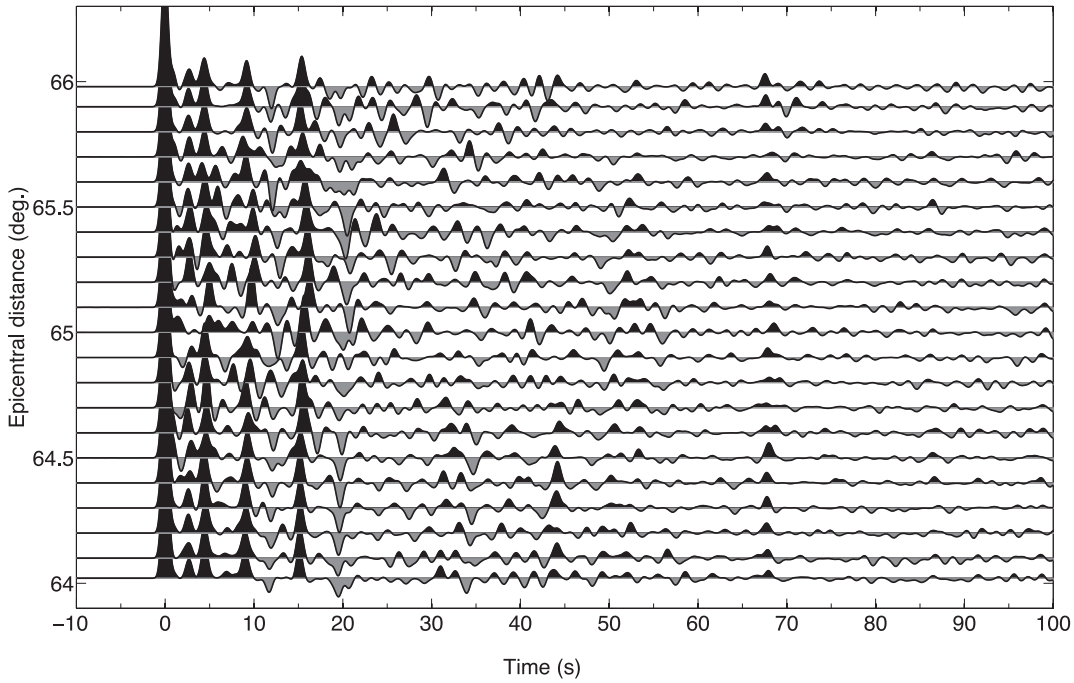

Figure 12. Receiver functions for the line of receivers shown in Fig. 1 when the topography of the Pyrenees is included.

4.1 Moho jump

We construct a very simplified model of the Pyrenean crust, with two crustal blocks separated by a vertical fault oriented E-W, which represents the North Pyrenean Fault. This fault is located in the middle of the grid, 65° away from the source. In the northern block, which represents the European crust, the crust is taken from iasp91 and is 35 km thick. In the southern block, which represents the Iberian crust, the crust is 55 km thick at the location of the vertical fault. In the southern block, crustal thickness varies smoothly towards the south to reach a value of 35 km at the southern edge of the grid. This smooth variation is described by a polynomial of degree 2. Figs 5 and 6 show snapshots of the vertical component of the total and scattered wavefields, respectively. The geometry of the Moho jump is also displayed. The scattered wavefield has been obtained by subtracting the wavefield in the reference spherical earth model from the total wavefield with the Moho jump. Particularly strong scattered waves are generated when the *PcP* and the P660s hit the fault. Figs 7 and 8 show the vertical and radial component synthetic seismograms for the same explosive source as before.

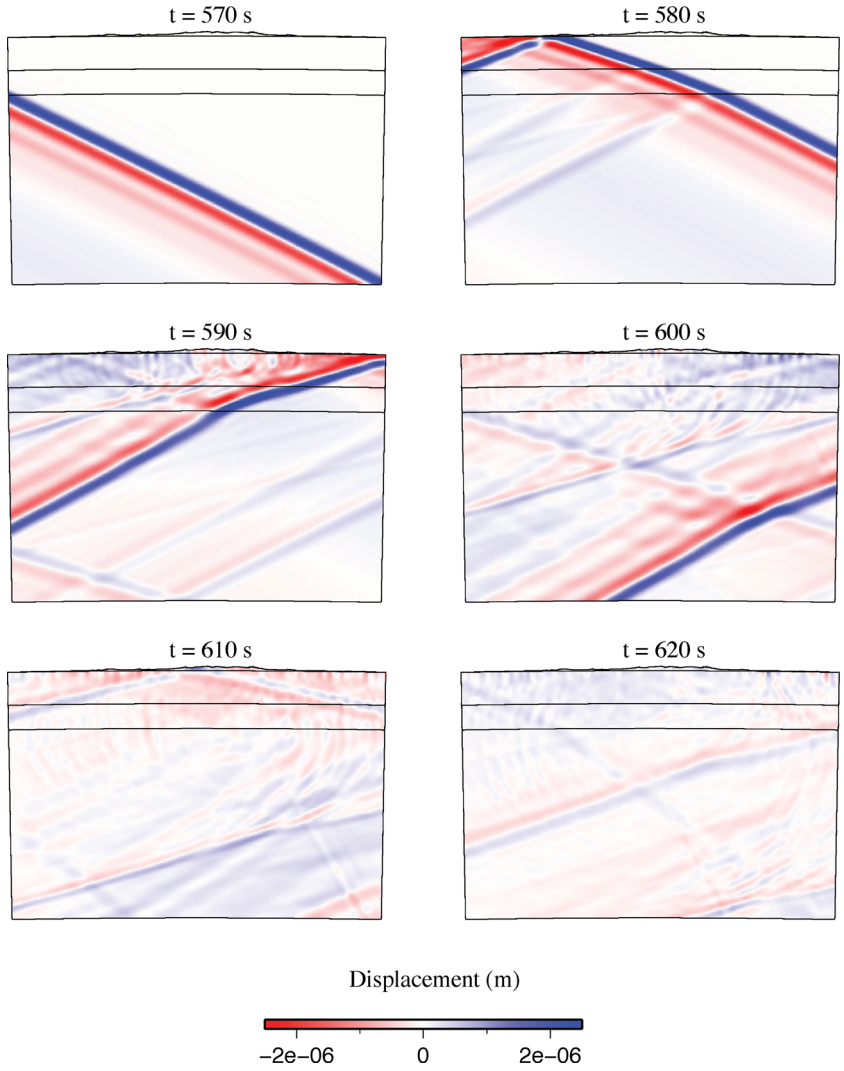

Figure 13. Snapshots of the vertical component of the total wavefield in the model with the surface topography of the Pyrenees observed in the vertical great-circle plane.

Note that there are no visible artificial reflections coming from the edges, even for the receivers located at the southern and northern ends of the profile, which are very close (0.2°) to the boundaries of the regional mesh. On the vertical components, the main effect of the Moho jump is observed on the PPmp and PPms phases, the hodochrones of which show a pronounced curvature between 64.0° and 65.4°, well beyond the vertical fault. Similar effects on the PPms are observed on the radial component section. In contrast, the effect of the Moho offset is more subtle on the Pms phase. Its onset is clearly delayed around 64.8° but is already back to normal at 65°. This is a consequence of the steeper incidence angle of the Pms phase compared to the *P* phase. All these features are more clearly observed on the receiver function profile as shown in Fig. 9. The Moho offset also generates scattered waves that radiate from the bottom part of the vertical fault. Another notable effect of the Moho offset is the deflection of the *P* and pP (and its pmP precursor) towards vertical incidence, which reduces their amplitudes on the radial component.

4.2 Topography of the free surface

Topography of the free surface also perturbs the seismic wavefield. To quantify this effect, we now introduce the topography of the Pyrenees extracted from etopo1 (http://www.ngdc.noaa.gov) in the top of the regional mesh (Fig. 1). The typical distance between two grid points at the surface is about 1200 m, while the sampling rate of topography in etopo1 is about 1.8 km.

Figs 10 and 11 show the vertical and radial components for synthetic seismograms recorded by the N–S line of receivers. Surface topography has a strong signature on both vertical and radial components. The topographic heights of the Pyrenees, located approximately in the middle of the profile, radiate energy both southwards and northwards, but the radiation is stronger in the forward propagation direction. These waves have a very large apparent slowness (around 30 s/deg) and are observed on both the vertical and radial components, which suggests that they are Rayleigh waves. These Rayleigh waves are clearly observed on the snapshots of the vertical component wavefield in the upper crust (Fig. 13). They produce a complex and coherent wavefield that trails the *P* wave front (Fig. 14). It is interesting to note that the part of the signals that is contaminated by these Rayleigh waves gets longer for larger distances from the centre of the range. Topographic effects are still strong in the seismograms at stations located more than 100 km outside the range. Conversions and reflections on internal discontinuities are clearly enhanced in the receiver function

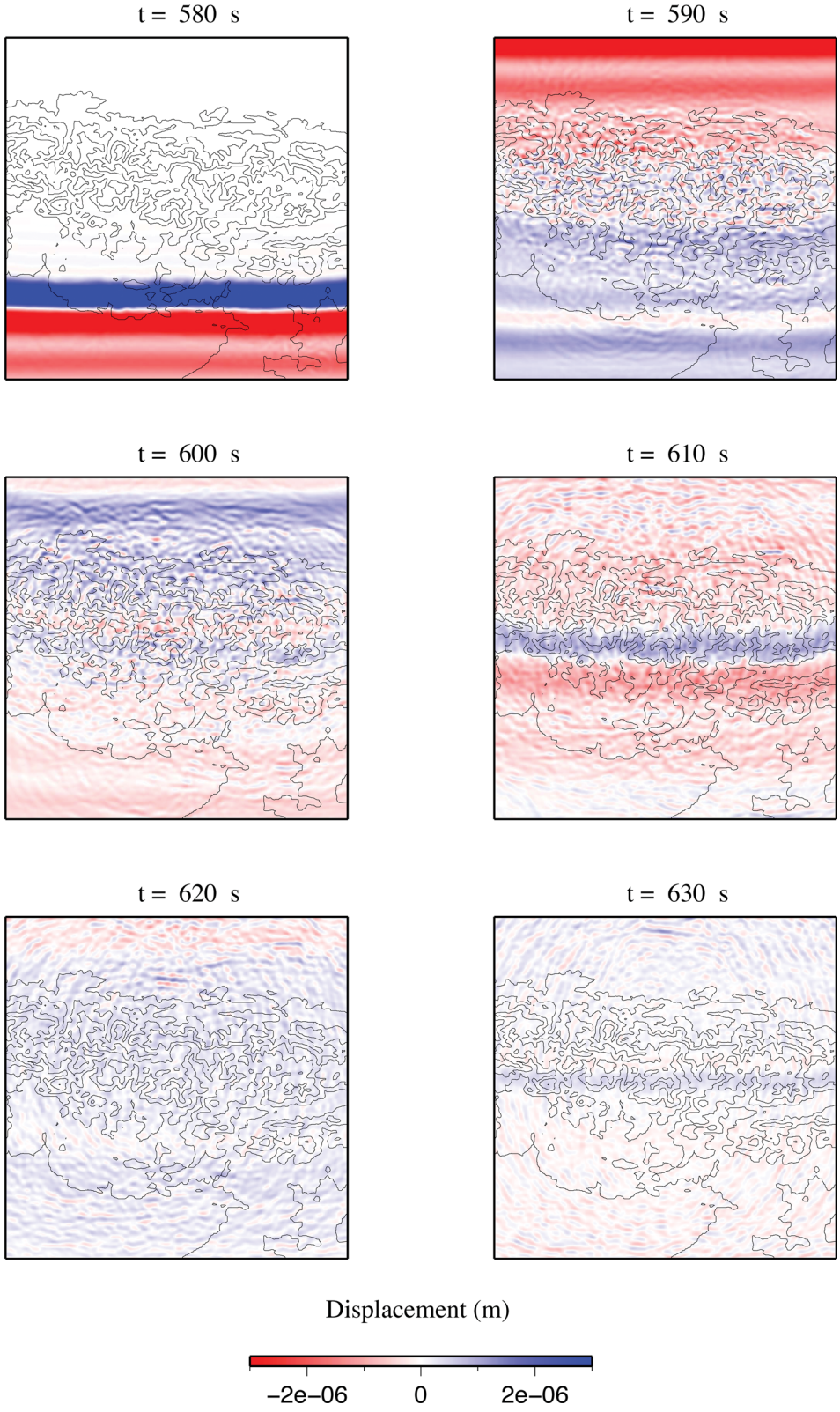

Figure 14. Snapshots of the vertical component of the total wavefield in the model with the surface topography of the Pyrenees observed at the free surface.

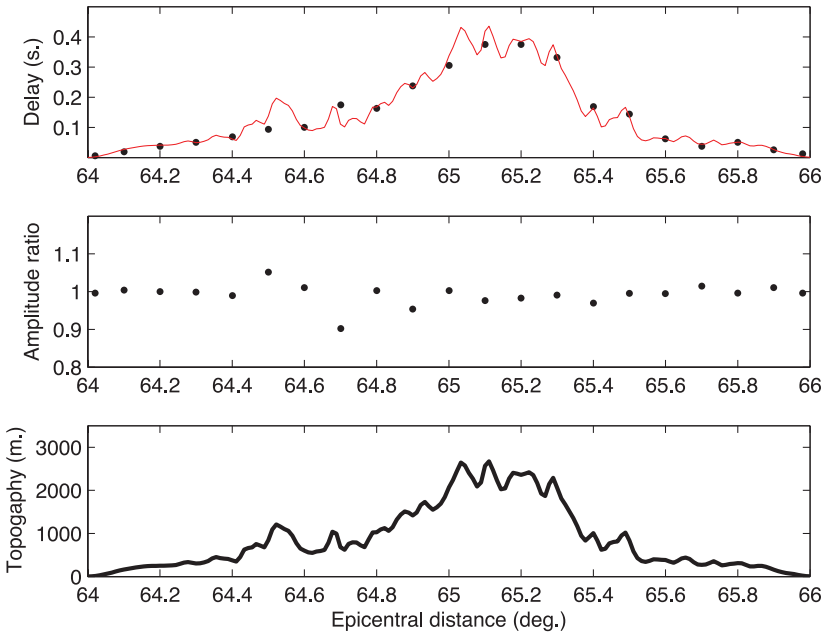

Figure 15. Perturbations of traveltimes (top), amplitudes (middle) and topography profile (bottom) along the receiver line. The red line in the top plot shows the topography corrections that are classically used in body wave tomography.

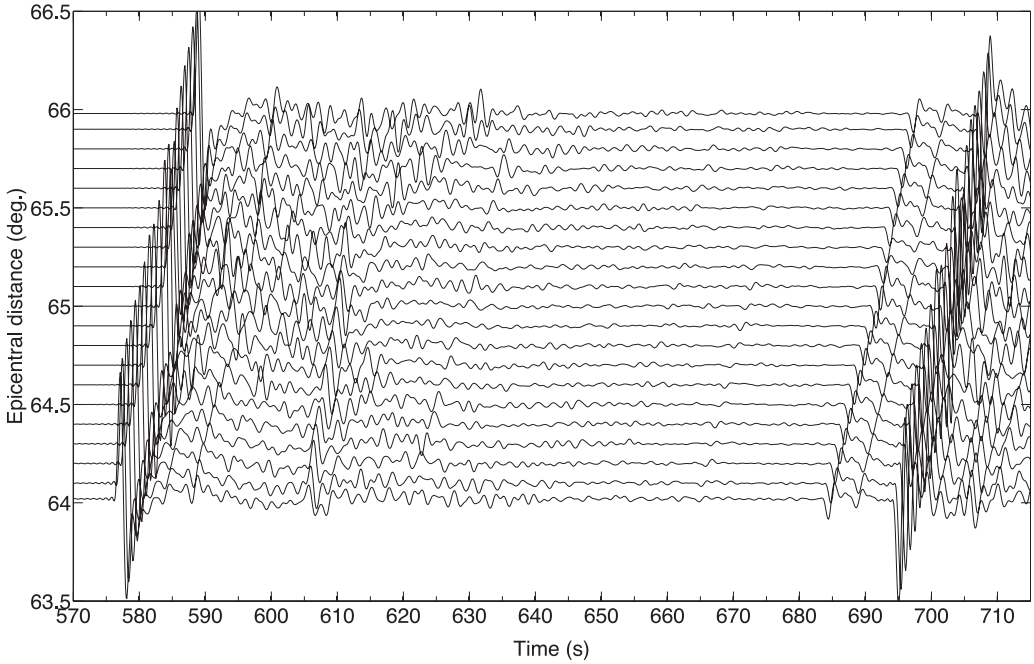

Figure 16. Vertical component synthetic seismograms in the model with both a 20 km Moho offset and the surface topography of the Pyrenees for an explosive source located at 600 km depth.

section (Fig. 12), the appearance of which is strikingly similar to what is typically obtained when analysing real data (e.g. Chevrot & Girardin 2000). A notable feature in the receiver function section is that both onsets and amplitudes of crustal multiples vary greatly from trace to trace. This results from the downward reflection on topography, which perturbs the length of reflection legs and hence the traveltime of reflected waves, and focuses/defocuses the reflected *P* wave front. These effects are difficult to predict because they result from the interference of the incident wavefield with topography around the bounce point, usually a few tens of kilometres away from the receiver. In contrast, perturbations of traveltimes and amplitudes produced by topography on the direct *P* wave are much smaller and more predictable. We measure these perturbations by correlating the synthetic seismograms for the model that includes the topography with those computed in iasp91 (Fig. 15). There is excellent agreement between the traveltime delays (black circles) and the topographic corrections (red line) that are classically used in global and regional body wave tomography. The amplitude perturbations of the direct *P* wave are rather small, generally smaller than 4 per cent, and not correlated to topography in a simple fashion.

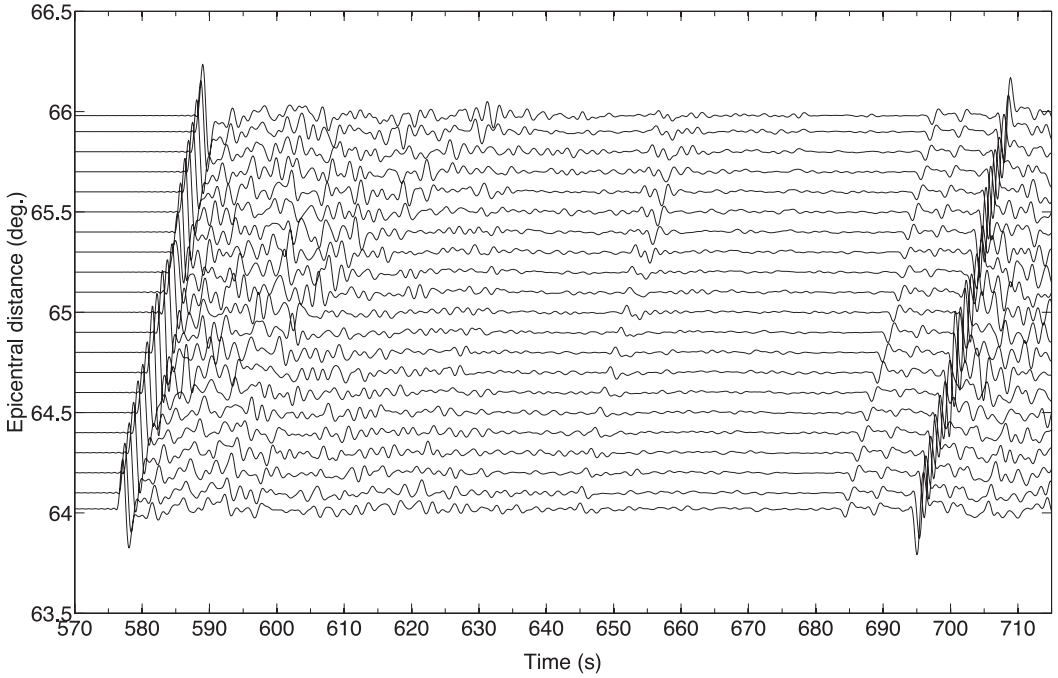

Figure 17. Radial component synthetic seismograms in the model with both a 20 km Moho offset and the surface topography of the Pyrenees for an explosive source located at 600 km depth.

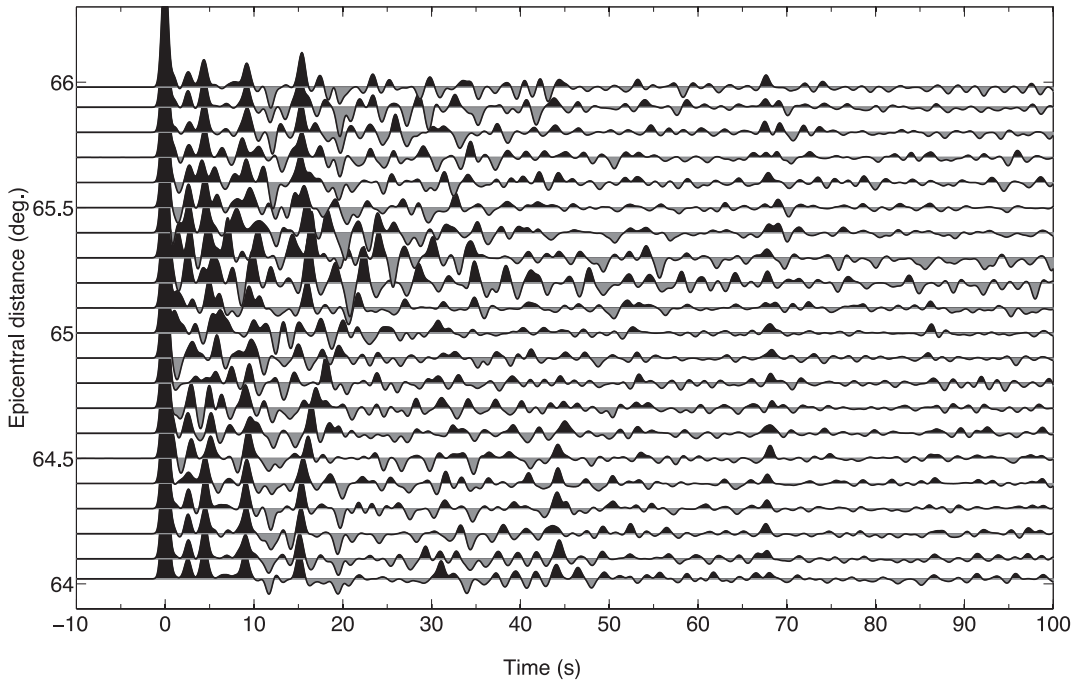

Figure 18. Receiver functions for the line of receivers shown in Fig. 1 when both the topography of the Pyrenees and a Moho offset are included.

4.3 Moho jump and topography of the free surface

Let us finally consider both the Moho jump and the topography of the free surface to investigate their combined effects. Figs 16 and 17 show the vertical and radial components for synthetic seismograms recorded by the N–S line of receivers. The curvatures of the PPmp and PPms phases are now barely visible owing to the strong amplitudes of Rayleigh waves produced by mode conversion on topography. Fig. 18 shows receiver functions for the line of receivers. Although this section has a noisier appearance, it is very similar to the receiver function section shown in Fig. 9. The deconvolution has the beneficial effect of concentrating energy on the pulses of the different arrivals, removing most of the signal-generated noise resulting from mode conversion on topography of the free surface, even before stacking.

5 DISCUSSION

Our waveform propagation modelling of short-period teleseismic *P* waves in 3-D regional media demonstrates that many coherent phases with different slownesses have significant contributions to the coda of the *P* wave. Since these phases have amplitudes comparable to those of waves scattered by 3-D heterogeneities, modelling the incident wavefield by considering a single incoming plane wave may lead to significant artefacts in the reconstruction of the underlying medium by waveform inversion. We also found that even in the rather simple models considered in this study, 3-D propagation effects are important. These effects would be even stronger for a backazimuth of the source outside the strike of the receiver profile. Our results thus undermine waveform modelling and inversion methods based upon simplified 2-D approaches and that consider an isolated and single incoming plane wave.

The conversions from *P* to Rayleigh waves at the free surface have a major imprint on seismograms, even far from the topographic heights of the range. In our simulations, these Rayleigh waves are still strong more than 100 km away from their source. We will perform more realistic simulations accounting for the effects of attenuation in the future. Nevertheless, these results are in good agreement with the few published detailed analyses of *P* coda. Characterization of seismic wave trains in the coda of the *P* wave is difficult because it requires utilizing small-aperture arrays, which explains why reliable reports of Rayleigh waves produced by scattering on topography are scarce in the literature. An example can be found in Bannister *et al.* (1990), where it is reported that receiver-end scattering in the region of the NORESS array is dominated by *P*-to-*Rg* conversions from two nearby topographic reliefs. Numerical simulations considering a vertically incoming plane *P* wave in a model that included a realistic topography for this region later showed evidence for strong conversions from *P* to Rayleigh waves on these two reliefs (Hestholm 1999). Since they are only a few hundred metres high, these results suggest, assuming that they are numerically correct, that mode conversion by topography can be important even outside elevated mountain ranges, and that they should be accounted for and modelled accurately.

Our modelling relied on topography model etopo1. Since we simulate waveforms with a wavelength of typically a few kilometres, this topographic model is probably sufficient. However, in the near future, we will perform benchmarks with the finer SRTM topographic model to confirm if this is really the case.

6 CONCLUSIONS

We have developed a hybrid method that couples the DSM, which is a global propagation method, with a regional 3-D SEM, for the simulation of short-period teleseismic *P* waves. We have benchmarked the method against DSM synthetics in the reference earth model iasp91. The hybrid method can incorporate all the complexity of the medium that may affect wave propagation inside the regional 3-D domain: lateral variations of isotropic and anisotropic elastic parameters, anelasticity, and topography of the free surface and internal discontinuities. In this study, we have also investigated the effects of topography of the free surface and the Moho. We have found that topography of the free surface has a major effect on seismic waveforms, not only at stations located in the mountain range but more surprisingly even more so at stations located in the plains at distances that can exceed 100 km. This suggests that it is important to account for topography effects in waveform modelling and inversion. The computations required only modest computational resources, opening the way for high-resolution imaging by waveform inversion. The computation of Fréchet derivatives with the adjoint method (e.g. Tromp *et al.* 2008) and their utilisation for waveform inversion will be presented in future work.

ACKNOWLEDGMENTS

This study was supported by the French Research Agency 'ANR blanc' program (project PYROPE, ANR-09-BLAN-0229), by the ANR 'Interdisciplinary Program on Application Software towards Exascale Computing for Global Scale Issues' program (SEISMIC IMAGING project, ANR-10-G8EX-002), and by INRIA Pau Bordeaux Sud-Ouest (MAGIQUE3D group). Some calculations were performed on the GENCI/CCRT/CEA 'Titane' computer. The authors thank Roland Martin and Qinya Liu for discussion, and Zhinan Xie for discussion about the absorbing conditions.

REFERENCES

Akçelic, V. *et al.*, 2003. High-resolution forward and inverse earthquake modeling on terascale computers, in *Proceedings of the ACM/IEEE Conference on Supercomputing,* Phoenix, AZ.

Aki, K., Christofferson, A. & Husebye, E.S., 1977. Determination of the three-dimensional seismic structures of the lithosphere, *J. geophys. Res.,* **82,** 277–296.

Al-Attar, D. & Woodhouse, J.H., 2008. Calculation of seismic displacement fields in self-gravitating earth models—applications of minor vectors and symplectic structure, *Geophys. J. Int.,* **175,** 1176–1208.

Alterman, Z., Jarosch, H. & Pekeris, C.L., 1959. Oscillations of the Earth, *Proc. R. Soc. Lond. A,* **252,** 80–95.

Audet, P., Bostock, M.G., Christensen, N.I. & Peacock, S.M., 2009. Seismic evidence for overpressured subducted oceanic crust and megathrust fault sealing, *Nature,* **457,** 76–78.

Bannister, S.C., Husebye, E.S. & Ruud, B.O., 1990. Teleseismic P coda analyzed by three-component and array techniques: determining location of topographic P-to-Rg scattering near the NORESS array, *Bull. seism. Soc. Am.,* **80,** 1969–1986.

Bielak, J. & Christiano, P., 1984. On the effective seismic input for nonlinear soil-structure interaction systems, *Earthq. Eng. Struct. Dyn.,* **12,** 107–119.

Bostock, M.G., Hyndman, R.D., Rondenay, S. & Peacock, S.M., 2002. An inverted continental Moho and serpentinization of the forearc mantle, *Nature,* **417,** 536–538.

Bostock, M.G., Rondenay, S. & Shragge, J., 2001. Multiparameter two-dimensional inversion of scattered teleseismic body waves 1. Theory for oblique incidence, *J. geophys. Res.,* **106,** 30 771–30 782.

Bouchon, M., Schultz, C.A. & Toksoz, M.N., 1996. Effect of three-dimensional topography on seismic motion, *J. geophys. Res.,* **101,** 5835–5846.

Burdick, S. *et al.*, 2008. Upper mantle heterogeneity beneath North America from travel time tomography with global and USArray transportable array data, *Seismol. Res. Lett.,* **79,** 384–392.

Capdeville, Y., Chaljub, E., Vilotte, J.P. & Montagner, J.P., 2003. Coupling the spectral element method with a modal solution for elastic wave propagation in global earth models, *Geophys. J. Int.,* **152,** 34–67.

Carrington, L., Komatitsch, D., Laurenzano, M., Tikir, M., Michéa, D., Le Goff, N., Snavely, A. & Tromp, J., 2008. High-frequency simulations of global seismic wave propagation using SPECFEM3D_GLOBE on 62 thousand processor cores, in *Proceedings of the ACM/IEEE Supercomputing SC'2008 Conference*.

Chapman, C.H. & Orcutt, J.A., 1985. The computation of body wave synthetic seismograms in laterally homogeneous media, *Rev. Geophys.,* **23,** 105–163.

Chevrot, S., Favier, N. & Komatitsch, D., 2004. Shear wave splitting in three-dimensional anisotropic media, *Geophys. J. Int.,* **159,** 711–720.

Chevrot, S. & Girardin, N., 2000. On the identification of reflected and converted waves from receiver functions, *Geophys. J. Int.,* **141,** 801–808.
Chevrot, S. & Zhao, L., 2007. Multi-scale finite-frequency Rayleigh wave tomography of the Kaapvaal craton, *Geophys. J. Int.,* **169,** 201–215.
Choukroune, P., Roure, F. & Pinet, B., 1990. Main results of the ECORS Pyrenees profile, *Tectonophysics,* **173,** 411–423.
Dahlen, F.A., Hung, S.H. & Nolet, G., 2000. Fréchet kernels for finite-frequency traveltimes—I. Theory, *Geophys. J. Int.,* **141,** 157–174.
Daignières, M., de Cabissole, B., Gallart, J., Hirn, A., Surinach, E. & Torne, E., 1989. Geophysical constraints on the deep structure along the ECORS Pyrenees line, *Tectonics,* **8,** 1051–1058.
Dziewonski, A.M. & Anderson, D.L., 1981. Preliminary reference Earth model, *Phys. Earth planet. Inter.,* **25,** 297–356.
Dziewonski, A.M., Chou, T.A. & Woodhouse, J.H., 1981. Determination of earthquake source parameters from waveform data for studies of global and regional seismicity, *J. geophys. Res.,* **86,** 2825–2852.
Falk, R. & Richter, G.R., 1999. Explicit finite element methods for symmetric hyperbolic equations, *SIAM J. Numer. Anal.,* **36,** 935–952.
Favier, N., Chevrot, S. & Komatitsch, D., 2004. Near-field influences on shear wave splitting and traveltime sensitivity kernels, *Geophys. J. Int.,* **156,** 467–482.
Fichtner, A., Kennett, B.L.N., Igel, H. & Bunge, H.P., 2008. Theoretical background for continental- and global-scale full-waveform inversion in the time-frequency domain, *Geophys. J. Int.,* **175,** 665–685.
Friederich, W. & Dalkolmo, J., 1995. Complete synthetic seismograms for a spherically symmetrical Earth by a numerical computation of the Green's function in the frequency-domain, *Geophys. J. Int.,* **122,** 537–550.
Fuchs, K. & Müller, G., 1971. Computation of synthetic seismograms with the reflectivity method and comparison with observation, *Geophys. J. R. astr. Soc.,* **23,** 417–433.
Fuji, N., Chevrot, S., Zhao, L., Geller, R.J. & Kawai, K., 2012. Finite-frequency structural sensitivities of short-period compressional body waves, *Geophys. J. Int.,* **190,** 522–540.
Geller, R.J. & Ohminato, T., 1994. Computation of synthetic seismograms and their partial derivatives for heterogeneous media with arbitrary natural boundary-conditions using the direct solution method, *Geophys. J. Int.,* **116,** 421–446.
Geller, R.J. & Takeuchi, N., 1995. A new method for computing highly accurate DSM synthetic seismograms, *Geophys. J. Int.,* **123,** 449–470.
Helmberger, D.V., 1974. Generalized ray theory for shear dislocations, *Bull. seism. Soc. Am.,* **64**(1), 45–64.
Hestholm, S., 1999. Three-dimensional finite difference viscoelastic wave modelling including surface topography, *Geophys. J. Int.,* **139,** 852–878.
Hu, F.Q., Hussaini, M.Y. & Rasetarinera, P., 1999. An analysis of the discontinuous Galerkin method for wave propagation problems, *J. Comput. Phys.,* **151,** 921–946.
Hung, S.H., Shen, Y. & Chiao, L.Y., 2004. Imaging seismic velocity beneath the Iceland hotspot; a finite-frequency approach, *J. geophys. Res.,* **109,** B08305, doi:10.1029/2003JB002889.
Kawai, K., Takeuchi, N. & Geller, R.J., 2006. Complete synthetic seismograms up to 2 Hz for transversely isotropic spherically symmetric media, *Geophys. J. Int.,* **164,** 411–424.
Kennett, B.L.N. & Engdahl, E., 1991. Travel times for global earthquake location and phase identification, *Geophys. J. Int.,* **105,** 429–465.
Komatitsch, D., Labarta, J. & Michéa, D., 2008. A simulation of seismic wave propagation at high resolution in the inner core of the Earth on 2166 processors of MareNostrum, *Lecture Notes Comput. Sci.,* **5336,** 364–377.
Komatitsch, D. & Tromp, J., 1999. Introduction to the spectral-element method for 3-D seismic wave propagation, *Geophys. J. Int.,* **139,** 806–822.
Komatitsch, D., Vinnik, L. & Chevrot, S., 2010. SHdiff/SVdiff discrepancy and seismic anisotropy in "D", *J. geophys. Res.,* **115,** B07312.
Langston, C.A., 1979. Structure under Mount Rainier, Washington, inferred from teleseismic body waves, *J. geophys. Res.,* **84,** 4749–4762.
Ligorria, J.P. & Ammon, C.J., 1999. Iterative deconvolution and receiver-function estimation, *Bull. seism. Soc. Am.,* **89,** 1395–1400.
Liu, Q. & Tromp, J., 2008. Finite-frequency sensitivity kernels for global seismic wave propagation based upon adjoint methods, *Geophys. J. Int.,* **174,** 265–286.
Martin, R., Komatitsch, D. & Gedney, S.D., 2008. A variational formulation of a stabilized unsplit convolutional perfectly matched layer for the isotropic seismic wave equation, *Comput. Model. Eng. Sci.,* **37,** 274–304.
Oliveira, S.P. & Seriani, G., 2011. Effect of element distortion on the numerical dispersion of spectral element methods, *Commun. Comput. Phys.,* **9,** 937–958.
Richards, P.G., 1973. Calculation of body waves, for caustics and tunnelling in core phases, *Geophys. J. astr. Soc.,* **35,** 243–264.
Ritsema, J., Deuss, A., van Heijst, H.J. & Woodhouse, J.H., 2011. S40RTS: a degree-40 shear-velocity model for the mantle from new Rayleigh wave dispersion, teleseismic traveltime and normal-mode splitting function measurements, *Geophys. J. Int.,* **184,** 1223–1236.
Rivière, B. & Wheeler, M.F., 2003. Discontinuous finite element methods for acoustic and elastic wave problems, *Contemp. Math.,* **329,** 271–282.
Roecker, S., Baker, B. & McLaughlin, J., 2010. A finite-difference algorithm for full waveform teleseismic tomography, *Geophys. J. Int.,* **181,** 1017–1040.
Roth, J.B., Fouch, M.J., James, D.E. & Carlson, R.W., 2008. Three-dimensional seismic velocity structure of the northwestern United States, *Geophys. Res. Lett.,* **35,** L15304, doi:10.1029/2008GL034669.
Sigloch, K., McQuarrie, N. & Nolet, G., 2008. Two-stage subduction history under North America inferred from multiple-frequency tomography, *Nature Geosci.,* **1,** 458–462.
Stacey, R., 1988. Improved transparent boundary formulations for the elastic wave equation, *Bull. seism. Soc. Am.,* **78,** 2089–2097.
Takeuchi, H. & Saito, M., 1972. Seismic surface waves, in *Methods of Computational Physics,* pp. 217–295, Academic Press, New York.
Tape, C., Liu, Q.Y., Maggi, A. & Tromp, J., 2009. Adjoint tomography of the Southern California crust, *Science,* **325,** 988–992.
Tromp, J., Komatitsch, D. & Liu, Q., 2008. Spectral-element and adjoint methods in seismology, *Commun. Comput. Phys.,* **3,** 1–32.
Wen, L. & Helmberger, D.V., 1998. A two-dimensional P-SV hybrid method and its application to modeling localized structures near the core-mantle boundary, *J. geophys. Res.,* **103,** 17 901–17 918.
Wilcox, L.C., Stadler, G., Burstedde, C. & Ghattas, O., 2010. A high-order discontinuous Galerkin method for wave propagation through coupled elastic-acoustic media, *J. Comput. Phys.,* **229,** 9373–9396.
Woodhouse, J.H. & Dziewonski, A.M., 1984. Mapping the upper mantle: three dimensional modelling of earth structure by inversion of seismic waveform, *J. geophys. Res.,* **89,** 5953–5986.
Yoshimura, C., Bielak, J., Hisada, Y. & Fernandez, A., 2003. Domain reduction method for three-dimensional earthquake modeling in localized regions. Part II: Verification and applications, *Bull. seism. Soc. Am.,* **93,** 825–840.
Zhao, L., Wen, L., Chen, L. & Zheng, T., 2008. A two-dimensional hybrid method for modeling seismic wave propagation in anisotropic media, *J. geophys. Res.,* **113,** B12307, doi:10.1029/2008JB005733.

SUPPORTING INFORMATION

Additional Supporting Information may be found in the online version of this article:

moho-jump.mov contains a movie showing the vertical component of the total (top) and scattered (bottom) wavefield observed in a vertical cross-section plane for the model with a 20 km Moho jump.
topo.mov contains a movie showing the vertical component of the total (top) and scattered (bottom) wavefield observed in a vertical cross-section plane for the model with the topography of the Pyrenees at the free surface.
surface.mov contains a movie showing the vertical component of the total wavefield observed on the free surface.
topo-moho-jump.mov contains a movie showing the vertical component of the total (top) and scattered (bottom) wavefield

observed in a vertical cross-section plane for the model with the topography of the Pyrenees at the free surface and a 20 km Moho jump (http://gji.oxfordjournals.org/lookup/suppl/doi:10.1093/gji/ggs006/-/DC1).